Published in final edited form as:
IEEE Trans Biomed Eng. 2014 February ; 61(2): 502–512. doi:10.1109/TBME.2013.2282775.

Creation and Characterization of an Ultrasound and CT Phantom for Non-invasive Ultrasound Thermometry Calibration

Chun-Yen Lai [Student Member, IEEE],
Department of Biomedical Engineering, University of California at Davis, Davis, CA 95616 USA

Dustin E. Kruse,
Department of Biomedical Engineering, University of California at Davis, Davis, CA 95616 USA

Katherine W. Ferrara [Fellow, IEEE], and
Department of Biomedical Engineering, University of California at Davis, Davis, CA 95616 USA

Charles F. Caskey [Member, IEEE]
Department of Biomedical Engineering, University of California at Davis, Davis, CA 95616 USA

Abstract

Ultrasound thermometry provides noninvasive two-dimensional (2-D) temperature monitoring, and in this paper, we have investigated the use of computed tomography (CT) radiodensity to characterize tissues to improve the accuracy of ultrasound thermometry. Agarose-based tissue-mimicking phantoms were created with glyceryl trioleate (a fat-mimicking material) concentration of 0, 10, 20, 30, 40, and 50%. The speed of sound (SOS) of the phantoms was measured over a temperature range of 22.1–41.1°C. CT images of the phantoms were acquired by a clinical dedicated breast CT scanner, followed by calculation of the Hounsfield units (HU). The phantom was heated with a therapeutic acoustic pulse (1.54 MHz), while RF data were acquired with a 10-MHz linear-array transducer. 2-D speckle tracking was used to calculate the thermal strain offline. The tissue dependent thermal strain parameter required for ultrasound thermometry was analyzed and correlated with CT radiodensity, followed by validation of the temperature prediction. Results showed that the change in SOS with the temperature increase was opposite in sign between the 0–10% and 20–50% trioleate phantoms. The inverse of the tissue dependent thermal strain parameter of the phantoms was correlated with the CT radiodensity ($R^2 = 0.99$). A blinded ultrasound thermometry study on phantoms with a trioleate range of 5–35% demonstrated the capability to estimate the tissue dependent thermal strain parameter and estimate temperature with error less than ~1°C. In conclusion, CT radiodensity may provide a method for improving ultrasound thermometry in heterogeneous tissues.

Index Terms

Computed tomography; thermal strain; thermometry; tissue-mimicking phantom; ultrasound

---

Corresponding author: Charles F. Caskey, Ph.D. cfcaskey@ucdavis.edu.

Color versions of one or more of the figures in this paper are available online at http://ieeexplore.ieee.org.

I. Introduction

Ultrasound has shown the potential to provide noninvasive two-dimensional (2-D) temperature monitoring, facilitating thermal dose examination over a spatial region. Several strategies have been developed for ultrasonic temperature measurement, such as tracking frequency shifts at two or more harmonic frequencies [1, 2], tracking the changes in backscattered energy [3], tracking the variation in the attenuation coefficient (usually applicable above 50°C) [4–6], and tracking the shift of the received echoes [7–12]. The echo-shift method is the most commonly used technique in which a temperature-based change in the speed of sound (SOS) and thermal expansion in the heated region are estimated. Based on this method, Simon *et al.* have shown that 2-D temperature estimation can be accomplished with an error within 0.5°C with high spatial resolution in a rubber tissue-mimicking phantom [11]. The estimation of echo displacement along A-lines is an alternative approach to detect temperature changes and has been shown to achieve a temperature accuracy that is less than 1°C on a rubber phantom or cow liver [10]. We have previously induced tissue heating using mild hyperthermia (~42°C) on an agarose phantom and implemented a 2-D speckle tracking algorithm for temperature estimation with a dual-mode therapeutic and imaging transducer coupled with a commercial ultrasound scanner that is capable of generating a temperature map offline. With motion compensation techniques, we demonstrated *in vivo* thermometry for monitoring mild hyperthermia in pre-clinical models with an average temperature error on the order of 1.0°C [7].

Commercial ultrasound scanners apply a fixed SOS which does not account for tissue dependence or changes in temperature. As a result, reconstructed images before and after temperature changes show virtual shifts of the speckle patterns in the depth direction of the images. The relationship between the incremental temperature change at depth z, $\Delta T(z)$, and the corresponding cumulative apparent displacement, $\Delta d(z)$, can be derived in the following expression [7, 9]:

$$\Delta T(z)=\frac{1}{\alpha(z)-\beta(z)}\cdot\frac{\partial}{\partial z}(\Delta d(z)) \quad (1)$$

where $\Delta d(z) = \delta t(z) \times c_0/2$, $\delta t(z)$ is the apparent time shift at depth z between echoes of successive frames and c_0 is the SOS which is assumed to be invariant with respect to z. $\alpha(z)$ is the linear coefficient of thermal expansion of the tissue at z, and $\beta(z)$ is the linear coefficient of SOS with respect to temperature. The $(\partial/\partial z)(\Delta d(z))$ is defined as thermal strain. The term $1/(\alpha(z)-\beta(z))$ is also represented as $k(z)$, which is a tissue dependent thermal strain parameter. $k(z)$ can be estimated by measuring $\alpha(z)$ and $\beta(z)$ of a material, or by evaluating the relationship between the temperature change and the thermal strain in (1).

An approximately linear relationship exists between thermal strain and temperature changes in the mild hyperthermia range [7]. Therefore, the inverse of the tissue dependent thermal strain parameter, $1/k(z)$, can be calculated by determining the slope of the linear regression curve of the strain as a function of temperature increase:

$$\frac{1}{k(z)}=\frac{\frac{\partial}{\partial z}(\Delta d(z))}{\Delta T(z)}=\frac{strain}{\Delta T(z)} \quad (2)$$

Further, assuming $k(z)$ is independent of z, (2) can be simplified as:

$$\frac{1}{k}=\frac{strain}{\Delta T} \quad (3)$$

By tracking the speckle patterns, the cumulative apparent displacement in the depth direction is calculated, and thermal strain is the derivative of the cumulative apparent displacement with respect to distance. After obtaining the tissue dependent thermal strain parameter, maps of temperature change can be estimated from ultrasound-based strain measurements.

Compared to thermocouples, ultrasound-assisted temperature measurement is noninvasive and can be applied to monitor the temperature distribution within a 2-D plane. However, knowledge of the tissue components is required for accurate thermometry. Specifically, the temperature coefficients for the SOS changes in an inverse fashion in fatty tissues as compared to high-water-content (nonfatty) tissues [8, 13–15] resulting in inaccurate temperature estimation in ultrasound thermometry if the tissue is not characterized. Computed tomography (CT) is an imaging modality where a series of X-ray projections are used to create a three-dimensional (3-D) map of the X-ray attenuation coefficients of the object being imaged. Hounsfield units (HU) provide a quantitative measurement that represents the CT radiodensity of a material referenced to water. This measurement is widely used to assess the composition of a body or tissue in the medical imaging field, and tissues have been characterized by their CT radiodensity within certain ranges [16]. Tissue segmentation in CT images has been successfully demonstrated based on pre-defined CT radiodensity ranges for protein-rich tissues, fat tissues and bones [17, 18]. Because of the potential of CT to quantify the fat content of tissue, CT examination prior to ultrasound thermometry may be used to improve temperature monitoring.

Combining CT-assisted tissue characterization with ultrasound thermometry requires a relationship between the CT radiodensity of materials and the tissue dependent thermal strain parameter. However, such a relationship cannot be derived directly, and the correlation has not been investigated. A tissue-mimicking phantom is a useful model to establish this relationship, in which homogeneous texture and tissue-related acoustic properties, such as acoustic absorption, attenuation and SOS, are readily achievable. Agarose gel is a suitable phantom material due to the spatial uniformity and high thermal stability of the cured gel. The high melting point of agarose keeps the phantom stable to a temperature of ~80°C [19], making agarose an ideal model for examining thermal therapy. Madsen *et al.* developed agarose-based tissue-mimicking phantoms in which evaporated milk was added to enhance absorption. Evaporated milk has an attenuation coefficient of ~0.8 dB/cm/MHz and SOS of 1547 m/s, thus a phantom was created by diluting the evaporated milk solution to an attenuation coefficient of 0.3–0.7 dB/cm/MHz. The SOS was compensated by adding n-propanol to achieve a final value near 1540 m/s [20], and graphite was used to adjust the attenuation coefficient as well as ultrasonic scattering properties [21].

The objective of this study is to examine the relationship between the tissue dependent thermal strain parameter and the CT radiodensity for a tissue-mimicking phantom with varied fat concentration. Glyceryl trioleate, a human-fat mimicking material, was used as the fat source in this study [22]. Agarose-based phantoms with 0 to 50% trioleate concentration were created with homogeneous texture, and mild hyperthermia was induced by a modified ultrasound scanner and a temperature feedback system. Here, temperature elevation was controlled in the range of 7–8°C to mimic a typical mild hyperthermia therapy. Radio-frequency (RF) images of heated phantoms were acquired with a linear array transducer with a second ultrasound scanner, and thermometry was performed off-line using a 2-D speckle tracking algorithm. CT radiodensity was measured by a dedicated breast CT scanner. Correlation of the tissue dependent parameter and the CT radiodensity were analyzed, followed by the evaluation of the temperature errors. Future applications of this study are discussed.

II. Materials and Methods

A. Phantom production

The phantom production procedure was modified from agarose-based evaporated-milk phantoms [20]. In this work, fat-free evaporated milk (Carnation, Nestle USA Inc., Solon, OH) was used, and therefore, the only fat source was glyceryl trioleate (Sigma-Aldrich Co. LLC., St. Louis, MO). The volume ratio of the fat-free evaporated milk, Dulbecco's phosphate-buffered saline (DPBS, Mediatech Inc., Manassas, VA), trioleate, and n-propanol (Sigma-Aldrich Co. LLC.) was 46:(50-x):x:4, respectively, where x denotes the volume ratio of the trioleate ranging from 0 to 50 (assuming total volume was 100). The amount of n-propanol was based on Madsen's recipe [20]. Agarose powder (OmniPur Agarose, EMD Chemicals Inc., Gibbstown, NJ) and silicon carbide (HSC1200, d50 = 6 μm, Superior Graphite, Chicago, IL) were 2% and 1.5%, respectively in a weight/total-volume ratio. In addition, a small amount of detergent (11% of the trioleate volume) (Palmolive Concentrated Dish Liquid, Colgate-Palmolive Company, New York, NY) was used to homogenize the emulsion. For higher trioleate concentrations, a modified method for phantom construction was devised to insure homogeneity. Although there is no absolute threshold on separating lower and higher trioleate concentration, the empirical boundary was determined in the 30% trioleate concentration.

1) Lower-trioleate concentration (0–30 v/v %)—First, fat-free evaporated milk, DPBS and agarose powder were mixed and microwaved until completely dissolved (90°C). The molten agarose solution was degassed for 5 minutes in a vacuum, followed by the addition of pre-heated trioleate (90°C). Gentle stirring was applied with a stir bar on a heating plate (Thermolyne, Barnstead International, Dubuque, IA) set to 90°C, and silicon carbide and detergent were then added. Stirring continued for 10 minutes to emulsify the trioleate and suspend the silicon carbide powder. The solution was then degassed for 5 minutes to remove air bubbles. n-Propanol was added after the degassing, and the heating plate was turned off to allow the molten agarose solution to cool naturally. Continuous stirring was applied until the solution reached 40°C, and the solution was then poured into a mold. Two sizes of molds were manufactured in this study for separate purposes: a smaller size mold (cubic-shape, 25.4 × 25.4 × 25.4 mm) designed for density, SOS, and CT radiodensity measurement and a larger size mold (rectangular-shape, 75 × 75 × 50 mm) for examination of Rayleigh speckle statistics and thermometry. The phantom solidified at room temperature (23°C) for at least 3 hours.

2) Higher-trioleate concentration (40–50 v/v %)—In this group, the phantom components were added in different order to prevent aggregation of silicon carbide during mixing. First, the trioleate and the silicon carbide powder were mixed, followed by heating to 90°C for 5 minutes on the heating plate. The mixture was then degassed for 5 minutes. In a second beaker, agarose powder, DPBS, and evaporated milk were mixed and heated to 90°C until completely dissolved, followed by degassing for 5 minutes. Solutions in the two beakers were then carefully combined, and gentle stirring was applied with the heat plate set to 90°C. Detergent and n-propanol were added to the solution, and heating was applied for another 5 minutes, followed by continuous stirring until the solution cooled to 40°C. The molten solution was then poured into the molds and solidified with the same procedure as in the lower-trioleate concentration group.

B. Analysis of phantom properties

1) Density—The phantom density was measured at 23°C. After the congealing process, the phantom was removed from the mold and immediately weighed by a balance (APX-602, Denver Instrument, Bohemia, NY). The volume of the phantom was the same as the known inner dimensions of the mold. Density was determined by dividing the weight by the volume of the phantoms. Consistent density was maintained throughout the study for all phantoms by preventing contact with water during measurements and encasing the phantoms after measurements.

2) SOS—Measurement of the SOS was conducted in a 3-L water bath filled with degassed deionized water [Fig. 1(a)]. Two 5-MHz single-element transducers (V309, Panametrics, Olympus NDT Inc., Waltham, MA) were positioned in a line on each side of the phantom, and transmission and reception of ultrasound pulses were performed by separate transducers. The phantom was wrapped with a layer of Saran wrap (S.C. Johnson & Son Inc., Racine, WI) to prevent diffusion of emulsified trioleate from the phantom surface to the water and the attenuation and SOS were verified to be unchanged.

The transmitted pulses were generated by a high power pulser (RPR 4000, Ritec Inc., Warwick, RI) with parameters of 20-cycle duration, 5-MHz center frequency, and 5-Hz pulse repetition frequency. The pulses were transmitted through a 150-ohm high power load (RT 150, Ritec Inc.) and a 16-dB attenuator (837 Attenuator, Kay Elemetrics Corp., Montvale, NJ) before driving the 5-MHz transducer. Signals passing through the phantom were received by another 5-MHz transducer and then filtered (band pass: 800 kHz – 10 MHz) and amplified (20 dB) in a broadband receiver (RPR 4000, Ritec Inc.) and displayed on an oscilloscope (DPO 4034, Tektronix Inc., Beaverton, OR). The signals captured by the oscilloscope were averaged 16 times, and then the shift of the one-way time-of-flight with and without the phantom in the acoustic path was compared to calculate the SOS of the phantom. In this method, the SOS of a phantom was calculated relative to the SOS of water at the same temperature. Given D and t_w as the distance between the two 5-MHz transducers and the one-way time-of-flight of the ultrasound signals travelling in water, respectively, the SOS of water, c_w, is calculated as:

$$c_w=\frac{D}{t_w} \quad (4)$$

Moreover, given d as the thickness of the phantom, Δt as the shift of the one-way time-of-flight of the signals defined by $\Delta t = t_p - t_w$, where t_p is the time-of-flight with the existence of a phantom, the SOS of the phantom c can be calculated by:

$$c=\frac{c_\mathrm{w}}{1+\Delta t\frac{c_w}{d}} \quad (5)$$

Calculation of the SOS of the phantoms with 0 to 50% trioleate concentration was conducted based on (5). For the SOS at different environmental temperatures, first, a heater and a stirrer (Model 71, PolyScience, Niles, IL) were used to adjust the water tank to the desired temperature, and then the SOS of the water and phantom was calculated. Temperatures of 22.1, 26.3, 30.9, 35.7, and 41.1°C were examined in this study. All of the measurements were conducted after thermal equilibrium between water bath and the phantoms was reached.

3) Rayleigh speckle statistics—The Rayleigh speckle statistics facilitate the evaluation of fully developed speckle, where Wagner *et al.* and Tuthill *et al.* defined signal-to-noise ratio (SNR) by dividing the mean by the standard deviation of the envelope of the echo of the transmitted signals, and a value of 1.91 is applied for comparison to determine whether fully developed speckle is observed [23, 24]. A phantom with entrapped air bubbles results in a SNR much less than 1.9. A Siemens Sonoline Antares ultrasound scanner (Siemens Medical Systems Inc., Issaquah, WA) and a commercial 10-MHz imaging transducer (VF10-5, Siemens Medical Systems Inc.) were used to acquire the RF images from the phantoms with image dimensions of 38.2 by 25 mm in the lateral and depth (axial) directions, respectively. The sampling rate in the depth direction was 60 MHz. All processes were performed in MATLAB (The MathWorks, Inc., Natick, MA): A Butterworth IIR filter (function *butter()*) with band limits of 8 and 12 MHz was applied to the RF image, and a 5.5× cubic spline interpolation (function *interp1()*) was applied in the lateral direction to create isotropic pixels in the RF image. The bias of the image was normalized by subtracting the average intensity followed by envelope detection using the Hilbert transform (function *hilbert()*) and attenuation compensation in the depth direction. Finally, the SNR of the image was calculated. Phantoms with trioleate concentration in the range of 0 to 50% were examined.

4) CT radiodensity—CT images of phantoms were acquired with a clinical dedicated breast CT scanner with an isotropic voxel dimension of 0.3 mm (breast CT scanner: X-ray tube current/voltage: 5 mA/80 kVp, 530 projections) [25]. Radiodensity was calculated by imaging a small cylinder of water during each CT imaging session. The average attenuation of the water cylinder, μ_{water}, was measured and used to convert linear attenuation values of the sample, μ_s, into a relative radiodensity using the following equation:

$$\mathrm{CT\,Radiodensity} = 1000 \times \frac{\mu_s - \mu_{water}}{\mu_{water}} \quad (6)$$

C. Ultrasound heating and thermometry

1) System design and experimental setup—Two Antares ultrasound scanners were combined in this study in which heating and RF image acquisition were performed by separate systems [Fig. 1(b)]. To generate a temperature increase (Antares #1), the scanner was equipped with modified system software [26], and a custom dual-mode multi-array transducer was used to generate a temperature elevation in the phantom [27]. Three parallel arrays were incorporated in the transducer, with two outer arrays (1.54 MHz) designed for therapeutic treatment (heating) and one center array (5.5 MHz) designed for imaging [26, 27]. The two therapeutic arrays were physically tilted at an angle of 10.2° towards the centerline to generate a co-focused beam geometry at 35 mm in the depth direction. Although dynamic focusing of the therapeutic arrays was achievable by electronic beamforming, a fixed insonation focus was used in this study. A PC equipped with a temperature feedback system was used to control Antares #1, in which temperature measurement from a needle thermocouple (HYP-1, Omega Engineering, Inc., Stamford, CT) was fed to a proportional-integral-derivative (PID) controller, and acoustic parameters were calculated and assigned through the Diagnostic User Interface (DUI). DUI is an Ethernet-based interface specific to the Siemens Antares systems that allows access to software and hardware variables to control the scanner. Single-beam unscanned insonation was used with a pulse length of 100 cycles and pulse repetition frequency of 5 kHz. The acoustic pressure and total acoustic power were measured in deionized degassed water as 2.0 MPa and 2.4 W by a hydrophone (HNZ-0400, Onda Corp., Sunnyvale, CA) and a radiation force balance (UPM-DT-1AV, Ohmic Instruments Co., Easton, MD), respectively. The control interface of the PC was implemented in LabVIEW (National Instruments Co., Austin, TX). On the image acquisition side (Antares #2), a commercial 10-MHz linear array transducer (VF10-5) was positioned such that the imaging plane was confocal to the therapeutic arrays of the dual-mode transducer. RF images were acquired from the Antares research interface, where pre-beamformed non-filtered data was recorded. It should be noted that although the dual-mode transducer has demonstrated the capability for image acquisition for ultrasound thermometry [7], we employed a higher-frequency imaging transducer in this study to investigate the influence of fat more accurately in the thermometry algorithm.

A phantom with a size of 75 × 75 × 50 mm was used in thermometry studies, where the dual-mode transducer and the 10-MHz transducer were placed perpendicular to one another on the adjacent sides of the phantom [Fig. 1(b)]. During insonation, a focus of 25 mm in depth was used for the therapeutic arrays (Antares #1), and the needle thermocouple was located 10 mm distal to the insonation focus to avoid possible thermocouple artifacts [28] and interference from the mechanical vibration occurring at the insonation focus. For data acquisition (Antares #2), RF images were acquired at a distance of 25 mm from the transducer surface with an image depth of 25 mm. The needle thermocouple was located ~37–40 mm from the surface of the 10-MHz transducer. The lateral span of the acquired image was 38.2 mm. At each acquisition, RF image frames with the same parameters were recorded three times followed by averaging to reduce noise.

2) Insonation and data acquisition—Before insonation, baseline acquisition was performed at room temperature. When insonation started, images were acquired by manually capturing each temperature increase of 1–2°C until the total number of acquisitions was ~6. Therapeutic insonation was turned off during image acquisition and then reactivated for heating to the next set-point temperature. With this protocol, images were acquired without interference from the therapeutic pulses.

3) Calculation of cumulative apparent displacement and thermal strain—Off-line processing was applied in this study, in which RF images at different accumulated temperatures were compared with the baseline RF image to generate cumulative apparent displacement maps. Procedures for calculating the cumulative apparent displacement maps and thermal strain were demonstrated previously [7], and a brief summary is described below. Data were processed in MATLAB and all of the parameters were optimized. The wavelength λ described here was based on the 10-MHz imaging frequency.

Step 1: Calculation of the cumulative apparent displacement: A region of interest (ROI) with a size of 2.3 × 2.3 λ was defined for the operation of the normalized 2-D speckle tracking between the baseline and the heated images. Correlation coefficient was calculated as [7, 9]:

$$CC(m,n)=\frac{\sum_i\sum_j\left(\left[SP_k(i,j)-\overline{SP_k}\right]\cdot\left[SP_s(i-m,j-n)-\overline{SP_s}\right]\right)}{\sqrt{\sum_i\sum_j\left(SP_k(i,j)-\overline{SP_k}\right)^2\cdot\sum_i\sum_j\left(SP_s(i-m,j-n)-\overline{SP_s}\right)^2}} \quad (7)$$

where *SP* denoted the speckle pattern of the ROI. SP_k and SP_s were kernel and search regions in the baseline and heated images, respectively. Both the kernel and the search region had the same size as the ROI. (i,j) described the pixels in the kernel and search region, and (m,n) was the searching range in the depth and lateral directions defined by $-\lambda/2<m<\lambda/2$ and $-1.4\lambda<n<1.4\lambda$, respectively. Comparing the peak location of $CC(m,n)$ with the location of SP_k, the shift was determined as the cumulative apparent displacement caused by heating. In this work, a 10× cubic spline interpolation (function *interp1()*) was applied on the matrix $CC(m,n)$ to achieve a 0.1-pixel precision in the cumulative apparent displacement maps.

Step 2: Filtering: A median filter (function *medfilt2()*) with a size of 4.6 × 4.6 λ was applied to the cumulative apparent displacement maps to reduce noise. The cumulative apparent displacement maps were then interpolated (cubic spline, function *interp1()*) by 5.5× in the lateral direction to achieve isotropic pixels, followed by smoothing with a 2-D circular-shape averaging filter (function *fspecial()*). The radius of the smoothing filter was 22.5 λ.

Step 3: Calculation of thermal strain: A Sobel operator modified based on GSobel by Jeny Rajan from the MATLAB Central open exchange community with a size of 15 × 15 λ was applied to the cumulative apparent displacement in the depth direction to calculate thermal strain. To quantify the thermal strain intensity at the thermocouple location, a square ROI centered at the thermocouple tip with a dimension of 13 × 13 λ was selected and the average strain intensity was calculated.

Step 4: Calibration curves: For a phantom with a unique trioleate concentration, RF images with differing accumulated temperature increases were processed by Steps 1–3, and the average thermal strain was plotted as a function of temperature increase. Linear regression was examined between thermal strain and temperature increases with zero incepts. Phantoms with different trioleate concentrations underwent the same procedure, and the slopes of the regression curves were determined as the inverse of the tissue dependent thermal strain parameter of the phantom with units of %/°C.

D. Data analysis and validation

All of the measurements, such as phantom density, change of SOS with temperature elevation, CT radiodensity, and the inverse of the tissue dependent thermal strain parameter, were correlated with trioleate concentration. The relationship between the tissue dependent thermal strain parameter and the CT radiodensity was analyzed.

For the validation of ultrasound thermometry, three additional phantoms with varied trioleate concentrations in a range of 5–35% were created and analyzed in a blinded study. In addition to the needle thermocouple, two bare-junction thermocouples (PT-6, Physitemp Instruments, Inc., Clifton, NJ) were placed on the image acquisition plane of the 10-MHz transducer for multi-point temperature validation. First, based on the results from the 0–50% trioleate phantoms, CT radiodensity of the phantoms was estimated, followed by prediction of the tissue dependent thermal strain parameter. Subsequently, the three phantoms were analyzed using the ultrasound thermometry algorithm described above in a blinded fashion, resulting in the tissue dependent thermal strain parameter associated with each phantom. Afterwards, the error between the predicted and measured tissue dependent thermal strain parameter was analyzed. The thermal strain maps were converted to 2-D temperature maps by the predicted tissue dependent parameter. The temperature at the three thermocouple locations was compared with the direct thermocouple measurements, with temperature error analysis performed to examine accuracy.

III. Results

A. Phantom properties

1) Density—Phantoms with trioleate concentration of 0 to 50% demonstrated densities of 1.06 ± 0.01 to 1.01 ± 0.01 g/cm^3, representing a decreasing trend along with the increasing trioleate concentration [Fig. 2(a) and Table I]. The densities of the 0% and 50%-trioleate phantoms were close to the densities of mammalian skeletal muscle and breast tissue described in literature, respectively [29, 30]. The density and trioleate concentration were linearly correlated (R^2 = 0.98).

2) SOS—In the temperature range from 22.1 to 41.1°C, phantoms with varied trioleate concentration showed different trends with respect to SOS [Fig. 2(b) and Table II]. The SOS in water was estimated to be 1470 and 1513 m/s at 22.1 and 41.1°C, respectively, and SOS was linearly correlated with temperature increase in this temperature range (2.3 m/s/°C, R^2 = 0.99). Phantoms with 0% and 10% trioleate concentration had increasing SOS with increasing temperature, while phantoms with trioleate concentration higher than 20% had decreasing SOS with increasing temperature [Fig. 2(b)]. The trioleate concentration for which the SOS did not respond to temperature change was estimated between 10 and 20%. At matched temperatures, phantoms with higher trioleate concentration showed lower SOS, and this phenomenon was more pronounced at higher temperatures. The ratio of change of SOS with respect to temperature elevation (ΔSOS/ΔT) as a function of trioleate concentration was 1.3 to −2.0 m/s/°C for the trioleate concentration of 0 to 50%, respectively (R^2 = 0.99, 0.96, 0.92, 0.99, 0.99, 0.99, respectively [Fig. 2(c) and Table II]). The value of ΔSOS/ΔT was linearly correlated with trioleate concentration within the trioleate range of 0 to 50%, demonstrating that trioleate linearly reduced the SOS in the concentration range we tested. The standard deviation of the SOS measurement was between 0.1 to 1.1 m/s (Table II).

3) Rayleigh speckle statistics—The SNR of the phantoms ranged from 1.88–1.95 (Table I), indicating that all of the phantoms were homogeneously constructed with fully established speckle.

4) CT radiodensity—The measured radiodensity was 71.1 ± 0.3 to −30.0 ± 0.4 HU for 0 to 50% trioleate concentration (Fig. 3 and Table I). A decreasing trend of the radiodensity was observed as the trioleate concentration increased. The radiodensity was linearly correlated with the trioleate concentration (R^2 = 0.99).

B. Thermal strain

The accumulated temperature increase among phantoms of varied trioleate concentration was 3.6 to 8.0°C, where typical phantoms achieved a 7–8°C elevation (Table III). Average strain intensities were negative in phantoms with 0 and 10% trioleate concentration, whereas positive strain intensities were obtained with trioleate concentrations of 30, 40, and 50% (Fig. 4).

In a typical case of negative strain, the 10%-trioleate phantom demonstrated a maximum negative strain intensity of −2.1 ± 0.1%, corresponding to an accumulated temperature increase of 8.0°C (Fig. 5). For a typical case of positive strain, the 30%-trioleate phantom showed a maximum positive strain intensity of 2.2 ± 0.1%, corresponding to an accumulated temperature increase of 5.7°C (Fig. 6). In the phantom with a 20% trioleate concentration, the average strain intensity was less than 0.4% (Fig. 4). The inverse of the tissue dependent thermal strain parameters (strain/ΔT) of the phantoms showed high linear correlation with trioleate concentration (Fig. 7 and Table I).

NIH-PA Author Manuscript
NIH-PA Author Manuscript

An increasing trend of strain/ΔT was observed as the trioleate concentration increased. Further, the inverse of the tissue dependent thermal strain parameter was highly correlated with the CT radiodensity, with the CT radiodensity decreasing as the inverse of the parameter increased (R^2 = 0.99, Fig. 8).

For the phantoms in the blinded study, the CT radiodensity was estimated based on the relationship of CT radiodensity vs. trioleate concentration obtained in Fig. 3. The tissue dependent thermal strain parameter was calculated from the relationship established in Fig. 8. After the blinded analysis was completed, the measured tissue dependent thermal strain parameter was compared with prediction, resulting in an error within the range of 0.01 to 0.08 %/°C (Table IV). A representative case using three temperature probes in a phantom undergoing a maximum temperature increase of ~7°C at the needle thermocouple location is demonstrated in Fig. 9. The predicted temperatures closely matched the measured temperatures over the insonation period [Fig. 9(c)], and the error between predicted temperature from thermal strain and the measured temperature from the thermocouples in all three phantoms was ~1°C, demonstrating the predictive power of the proposed method in this study (Tables IV and V).

IV. Discussion and Conclusion

In this study, we have successfully constructed agarose-based tissue-mimicking phantoms with varied trioleate concentration and examined the relationship between the tissue dependent thermal strain parameter, $k(z)$, and the CT radiodensity. The validation experiment demonstrates that the methodology in this study is capable of measuring the tissue dependent thermal strain parameter of phantoms with varied fat content to generate accurate temperature maps with ultrasound thermometry. Although the literature reports 1°C accuracy in ultrasound thermometry using systems calibrated for a single-material phantom or tissue [7, 10, 11], our study proposes a method that can enable ultrasound thermometry in heterogeneous materials with opposite temperature coefficients of the SOS (here, a significant concentration of fat was incorporated in an agarose phantom). The accuracy of this method is sensitive to the absolute quantitation of CT radiodensity and can be further improved by improving the consistency and precision of CT scanners. In brief, ultrasound thermometry is inaccurate when being applied to a tissue with an unknown fat concentration. Through this study, a relationship between $k(z)$ and the CT radiodensity was established that could increase the accuracy of ultrasound thermometry.

The CT radiodensity is a quantitative scale in which the composition of an object can be determined based on the combined linear attenuation coefficient. With the addition of CT to ultrasound, tissues with a varied CT radiodensity can be distinguished [17] and thus temperature changes in different regions in the tissue can be estimated more accurately by ultrasound. The method presented here relies on precise calculation of the HU in tissue, which we achieved using a water reference. Cone beam CT scanners, such as the scanner used in our study or frequently in an interventional radiology suite, typically display relative linear attenuation values rather than HU. However, quantitative HU measurements can be achieved with cone beam CT with an error below 5% [31, 32]. In the future, CT examination prior to therapeutic ultrasound treatments can offer both structural and compositional information for a tissue, and the safety and efficacy of treatment could be improved.

The decrease in CT radiodensity with increasing trioleate concentration indicates that glyceryl trioleate has a smaller linear attenuation coefficient than water in X-ray radiography (Fig. 3). According to the results, phantoms with 0 and 10% trioleate concentration have radiodensity of 71.1 ± 0.3 and 54.1 ± 0.3 HU, respectively. Muscle and soft tissue (e.g., liver) contain 3–10% fat and have a typical radiodensity of ~10 to 50 HU [33]. Therefore, our phantoms with a trioleate percentage of 0–10% have a similar radiodensity to soft tissue. Moreover, extrapolating the linear regression curve in Fig. 3 to 100% fat concentration results in a radiodensity of ~−130 HU, which falls in the range of fat (−10 to −150 HU) [33], indicating that this phantom has a realistic radiodensity over an extended range of fat concentration.

The threshold for the fat concentration at which strain and SOS are unchanged with increasing temperature must be determined to optimize thermal therapy. In this work, a phantom with a 20% trioleate had insignificant strain, and very small changes in SOS were observed in the temperature range between 22.1 and 41.1°C. Mild hyperthermia frequently requires a temperature between 37 and 42°C, thus accurate thermometry in heterogeneous tissue in this temperature range is important.

The rate of temperature increase at the thermocouple location was lower in the phantoms with high trioleate concentration, particularly in the 50%-trioleate phantom. The 2-D temperature maps also showed a gradual shift in the location of the peak temperature toward the surface of the therapeutic transducer as the trioleate concentration increased (data not shown). Although focusing of the insonation beam might be altered with changes in the SOS and refractive index associated with varied trioleate concentration, the high attenuation coefficient resulting from high trioleate concentration may have contributed to this effect. We have examined the attenuation coefficient of the phantoms with trioleate concentration from 0 to 50% under 5-MHz frequency insonation, and coefficients of 0.4 to 1.4 dB/cm/MHz were measured, respectively. As a result, temperature elevation in deeper tissues may be reduced if high attenuating materials reside between the transducer and the target. Therefore, thermal mapping of the focus and proximal tissues are both important.

Separation of the phantom production procedures into higher and lower-trioleate concentration groups was required to minimize the aggregation of silicon carbide and generation of air bubbles resulting from the highly viscous mixture of agarose, evaporated milk, trioleate, and silicon carbide powder. Optimized procedures are required in each case to homogenize the suspension of silicon carbide powder. Using the procedures provided in this paper, phantoms with a sufficiently homogeneous texture were achieved.

Ultrasound thermometry enables 2-D temperature mapping and is helpful for guiding therapeutic ultrasound, offering the benefits of real-time thermometry at a low cost. Optimization of ultrasound thermometry is especially important for thermal therapies, such as mild hyperthermia, activatable temperature sensitive drugs [34], and ablation therapies [35]. Particularly in cancer therapies, patients frequently have CT image sets available, and these images could be registered with ultrasound for this purpose. With the recent development of commercial combined CT/US [36–39], the fusion between CT and ultrasound provides a method to identify intervening tissues between a transducer and its target. The methodology developed in this study provides the possibility to accurately calculate a 2-D temperature map according to tissue characterization (including structural and compositional) from a pre-acquired CT scan.

Acknowledgments

The authors would like to thank Dr. John M. Boone of the Department of Biomedical Engineering in the University of California at Davis for their kind offer of the dedicated breast CT scanner. They would also like to thank the NIH for their support for this project under NIHR01CA134659 and R01CA103828.

References

1. Seip R, Ebbini ES. Noninvasive estimation of tissue temperature response to heating fields using diagnostic ultrasound. IEEE Trans Biomed Eng. Aug; 1995 42(8):828–839. [PubMed: 7642197]
2. Amini AN, Ebbini ES, Georgiou TT. Noninvasive estimation of tissue temperature via high-resolution spectral analysis techniques. IEEE Trans Biomed Eng. Feb; 2005 52(2):221–228. [PubMed: 15709659]
3. Arthur RM, Straube WL, Starman JD, et al. Noninvasive temperature estimation based on the energy of backscattered ultrasound. Med Phys. Jun; 2003 30(6):1021–1029. [PubMed: 12852524]
4. Damianou CA, Sanghvi NT, Fry FJ, et al. Dependence of ultrasonic attenuation and absorption in dog soft tissues on temperature and thermal dose. J Acoust Soc Am. Jul; 1997 102(1):628–634. [PubMed: 9228822]
5. Clarke RL, Bush NL, Ter Haar GR. The changes in acoustic attenuation due to in vitro heating. Ultrasound Med Biol. Jan; 2003 29(1):127–135. [PubMed: 12604124]
6. Towa RT, Miller RJ, Frizzell LA, et al. Attenuation coefficient and propagation speed estimates of rat and pig intercostal tissue as a function of temperature. IEEE Trans Ultrason Ferroelectr Freq Control. Oct; 2002 49(10):1411–1420. [PubMed: 12403142]
7. Lai CY, Kruse DE, Caskey CF, et al. Noninvasive thermometry assisted by a dual-function ultrasound transducer for mild hyperthermia. IEEE Trans Ultrason Ferroelectr Freq Control. Dec; 2010 57(12):2671–2684. [PubMed: 21156363]
8. Huang SW, Kim K, Witte RS, et al. Inducing and Imaging thermal strain using a single ultrasound linear array. IEEE Trans Ultrason Ferroelectr Freq Control. Sep; 2007 54(9):1718–1720. [PubMed: 17941376]
9. Abolhassani MD, Norouzy A, Takavar A, et al. Noninvasive temperature estimation using sonographic digital images. J Ultrasound Med. Feb; 2007 26(2):215–222. [PubMed: 17255183]
10. Seip R, VanBaren P, Cain CA, et al. Noninvasive real-time multipoint temperature control for ultrasound phased array treatments. IEEE Trans Ultrason Ferroelectr Freq Control. Nov; 1996 43(6):1063–1073.
11. Simon C, VanBaren P, Ebbini ES. Two-dimensional temperature estimation using diagnostic ultrasound. IEEE Trans Ultrason Ferroelectr Freq Control. Jul; 1998 45(4):1088–1099. [PubMed: 18244264]
12. Liu D, Ebbini ES. Real-time 2-D temperature imaging using ultrasound. IEEE Trans Biomed Eng. Jan; 2010 57(1):12–16. [PubMed: 19884075]
13. Arthur RM, Straube WL, Trobaugh JW, et al. Non-invasive estimation of hyperthermia temperatures with ultrasound. Int J Hyperthermia. Sep; 2005 21(6):589–600. [PubMed: 16147442]
14. Pernot M, Tanter M, Bercoff J, et al. Temperature estimation using ultrasonic spatial compound imaging. IEEE Trans Ultrason Ferroelectr Freq Control. May; 2004 51(5):606–615. [PubMed: 15217237]

15. Miller NR, Bamber JC, Meaney PM. Fundamental limitations of noninvasive temperature imaging by means of ultrasound echo strain estimation. Ultrasound Med Biol. Oct; 2002 28(10):1319–1333. [PubMed: 12467859]
16. Yoshizumi T, Nakamura T, Yamane M, et al. Abdominal fat: standardized technique for measurement at CT. Radiology. Apr; 1999 211(1):283–286. [PubMed: 10189485]
17. Caskey CF, Hlawitschka M, Qin S, et al. An open environment CT-US fusion for tissue segmentation during interventional guidance. PLoS One. Nov.2011 6(11):e27372. [PubMed: 22132098]
18. Nelson TR, Cervino LI, Boone JM, et al. Classification of breast computed tomography data. Med Phys. Mar; 2008 35(3):1078–1086. [PubMed: 18404942]
19. Madsen EL, Zagzebski JA, Frank GR. Oil-in-gelatin dispersions for use as ultrasonically tissue-mimicking materials. Ultrasound Med Biol. 1982; 8(3):277–287. [PubMed: 7101576]
20. Madsen EL, Frank GR, Dong F. Liquid or solid ultrasonically tissue-mimicking materials with very low scatter. Ultrasound Med Biol. May; 1998 24(4):535–542. [PubMed: 9651963]
21. Madsen EL, Zagzebski JA, Banjavie RA, et al. Tissue mimicking materials for ultrasound phantoms. Med Phys. Sep-Oct;1978 5(5):391–394. [PubMed: 713972]
22. Kotzki PO, Buyck D, Hans D, et al. Influence of fat on ultrasound measurements of the os calcis. Calcif Tissue Int. Feb; 1994 54(2):91–95. [PubMed: 8012877]
23. Wagner RF, Smith SW, Sandrik JM, et al. Statistics of Speckle in Ultrasound B-Scans. IEEE Trans Sonics Ultrason. May; 1983 30(3):156–163.
24. Tuthill TA, Sperry RH, Parker KJ. Deviations from Rayleigh statistics in ultrasonic speckle. Ultrason Imaging. Apr; 1988 10(2):81–89. [PubMed: 3057714]
25. Boone JM, Nelson TR, Lindfors KK, et al. Dedicated breast CT: radiation dose and image quality evaluation. Radiology. Dec; 2001 221(3):657–667. [PubMed: 11719660]
26. Kruse DE, Lai CY, Stephens DN, et al. Spatial and temporal-controlled tissue heating on a modified clinical ultrasound scanner for generating mild hyperthermia in tumors. IEEE Trans Biomed Eng. Jan; 2010 57(1):155–166. [PubMed: 20064754]
27. Stephens DN, Kruse DE, Ergun AS, et al. Efficient array design for sonotherapy. Phys Med Biol. Jul; 2008 53(14):3943–3969. [PubMed: 18591737]
28. Waterman FM, Leeper JB. Temperature artifacts produced by thermocouples used in conjunction with 1 and 3 MHz ultrasound. Int J Hyperthermia. Mar-Apr;1990 6(2):383–399. [PubMed: 2324577]
29. Mendez J, Keys A. Density and composition of mammalian muscle. Metabolism. 1960; 9(2):184–188.
30. Duck, FA. Physical properties of tissue. San Diego, CA: Academic Press Inc; 1990. Mechanical properties of tissue; p. 228-229.
31. Mah P, Reeves TE, McDavid WD. Deriving Hounsfield units using grey levels in cone beam computed tomography. Dentomaxillofac Radiol. Sep; 2010 39(6):323–335. [PubMed: 20729181]
32. Yang K, Kwan A, Burkett G, et al. Hounsfield units calibration with adaptive compensation of beam hardening for a dose limited breast CT system. Med Phys. 2006; 33:1997.
33. Terrier, F.; Grossholz, M.; Becker, CD. Spiral CT of the abdomen. Springer; 2000. p. 554
34. Needham D, Anyarambhatla G, Kong G, et al. A new temperature-sensitive liposome for use with mild hyperthermia: characterization and testing in a human tumor xenograft model. Cancer Res. Mar; 2000 60(5):1197–1201. [PubMed: 10728674]
35. Crocetti L, Lencioni R, Debeni S, et al. Targeting liver lesions for radiofrequency ablation: an experimental feasibility study using a CT-US fusion imaging system. Invest Radiol. Jan; 2008 43(1):33–39. [PubMed: 18097275]
36. Jung EM, Schreyer AG, Schacherer D, et al. New real-time image fusion technique for characterization of tumor vascularisation and tumor perfusion of liver tumors with contrast-enhanced ultrasound, spiral CT or MRI: first results. Clin Hemorheol Microcirc. 2009; 43(1–2):57–69. [PubMed: 19713601]
37. Sandulescu DL, Dumitrescu D, Rogoveanu I, et al. Hybrid ultrasound imaging techniques (fusion imaging). World J Gastroenterol. Jan; 2011 17(1):49–52. [PubMed: 21218083]

38. Ewertsen C. Image fusion between ultrasonography and CT, MRI or PET/CT for image guidance and intervention - a theoretical and clinical study. Dan Med Bull. Sep.2010 57(9):B4172. [PubMed: 20816020]

39. Stang A, Keles H, Hentschke S, et al. Real-time ultrasonography-computed tomography fusion imaging for staging of hepatic metastatic involvement in patients with colorectal cancer: initial results from comparison to US seeing separate CT images and to multidetector-row CT alone. Invest Radiol. Aug; 2010 45(8):491–501. [PubMed: 20458251]

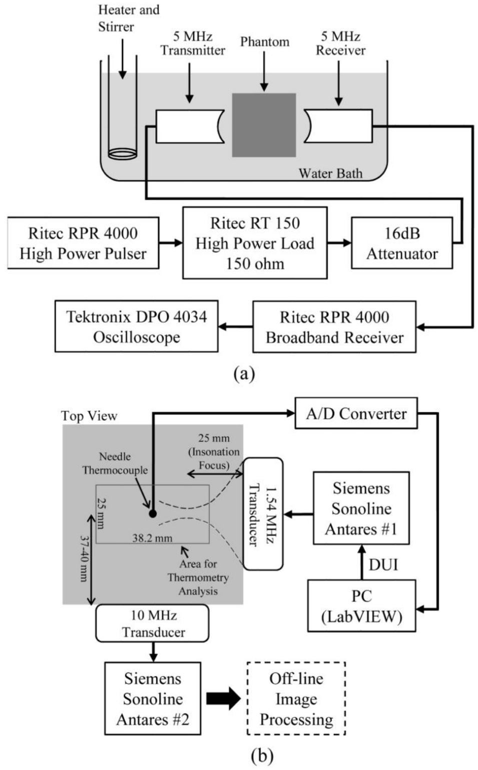

Fig. 1.
Experimental system for SOS measurement (a) and ultrasound thermometry (b). (a) Two 5-MHz transducers were positioned axially in a 3-L water tank filled with degassed deionized water. A 5-MHz, 20-cycle pulse was used for calculation of SOS of the phantoms. (b) In the thermometry experiments, single-beam insonation was generated by the dual-mode transducer (on Antares #1). RF data acquisition was performed by a 10-MHz linear-array transducer (on Antares #2) with dimensions of 38.2 (lateral) × 25 (depth) mm. Off-line data processing was applied for cumulative apparent displacement calculation and thermal strain analysis.

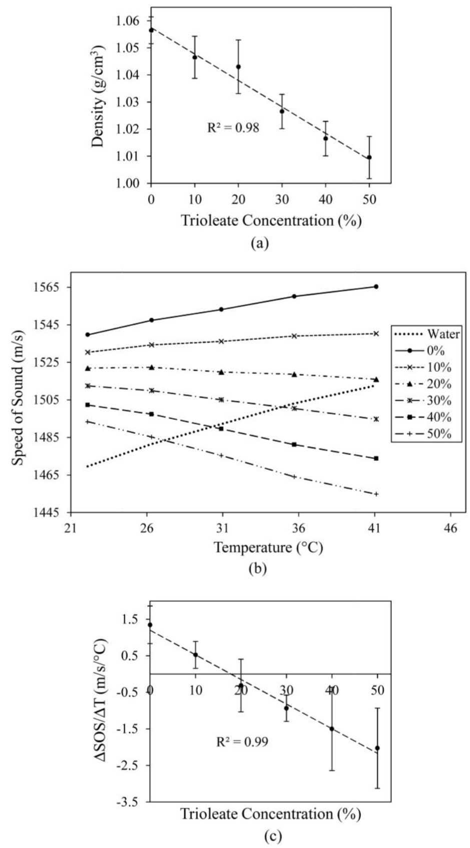

Fig. 2.

Density and SOS of the phantoms. (a) Density as a function of trioleate concentration. A decreasing trend of density was observed with increasing trioleate concentration. (n = 3, error bars show one standard deviation.) (b) SOS as a function of temperature for the phantoms with 0 to 50% trioleate concentration. A temperature range of 22.1 to 41.1°C was examined, with the SOS of water as a reference. (n = 4. See Table II for standard deviation.) (c) The change of SOS with °C increased (ΔSOS/ΔT) as a function of trioleate concentration. A ratio of 1.3 to −2.0 m/s/°C for trioleate concentrations from 0 to 50% was observed. (n = 4, error bars show one standard deviation.)

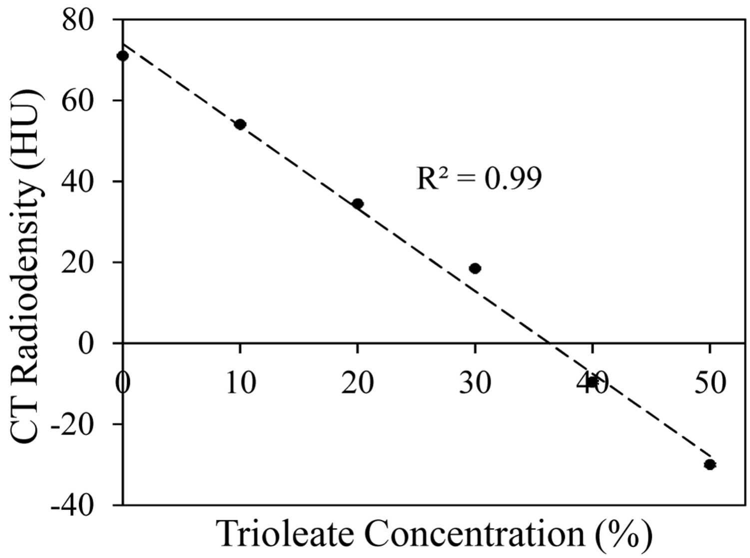

Fig. 3.
CT radiodensity of phantoms as a function of trioleate concentration. Houns-field unit was calculated from the CT images as 71.1 ± 0.3 to −30 ± 0.4 HU for 0 to 50% trioleate concentration, respectively. (n = 20, error bars show one standard deviation.)

NIH-PA Author Manuscript
NIH-PA Author Manuscript

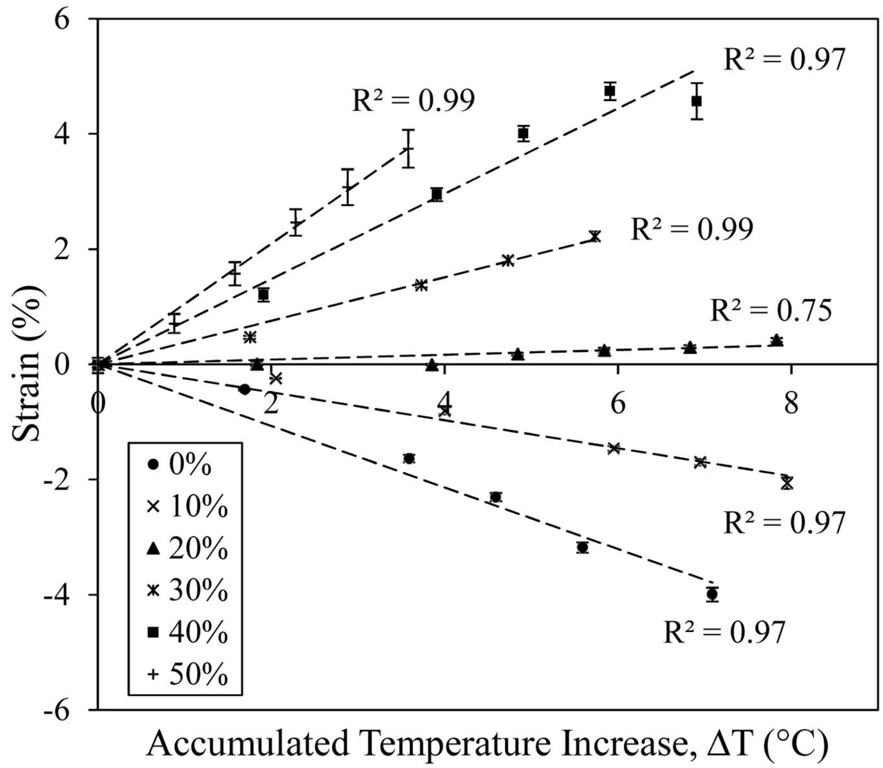

Fig. 4.

Strain as a function of accumulated temperature increase for differing trioleate concentrations. The phantom with 20% trioleate had the smallest change in strain with increasing temperature. Linear correlations were observed between strain and accumulated temperature increase for all of the phantoms. Error bars show one standard deviation calculated from the 13 × 13 λ ROI shown in Figs. 5–6.

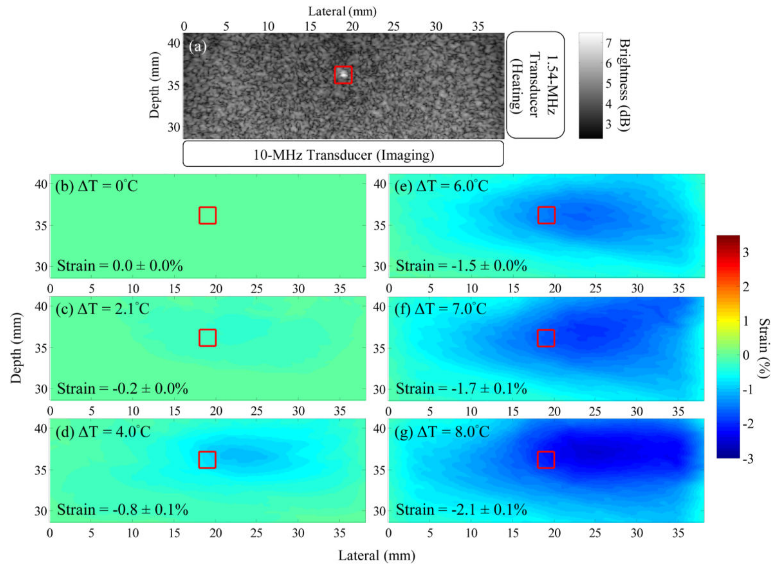

Fig. 5.

B mode image and thermal strain maps of the 10%-trioleate phantom. The square in each sub-figure represents the ROI (13 × 13 λ in 10-MHz imaging frequency) for calculating average strain intensity and standard deviation. The needle thermocouple is shown as a bright spot in the B mode image (a) and is centered in the square region. The orientation of the maps was the same as the experimental setup in Fig. 1(b), with the regions close to both transducers cropped for convenient visualization.

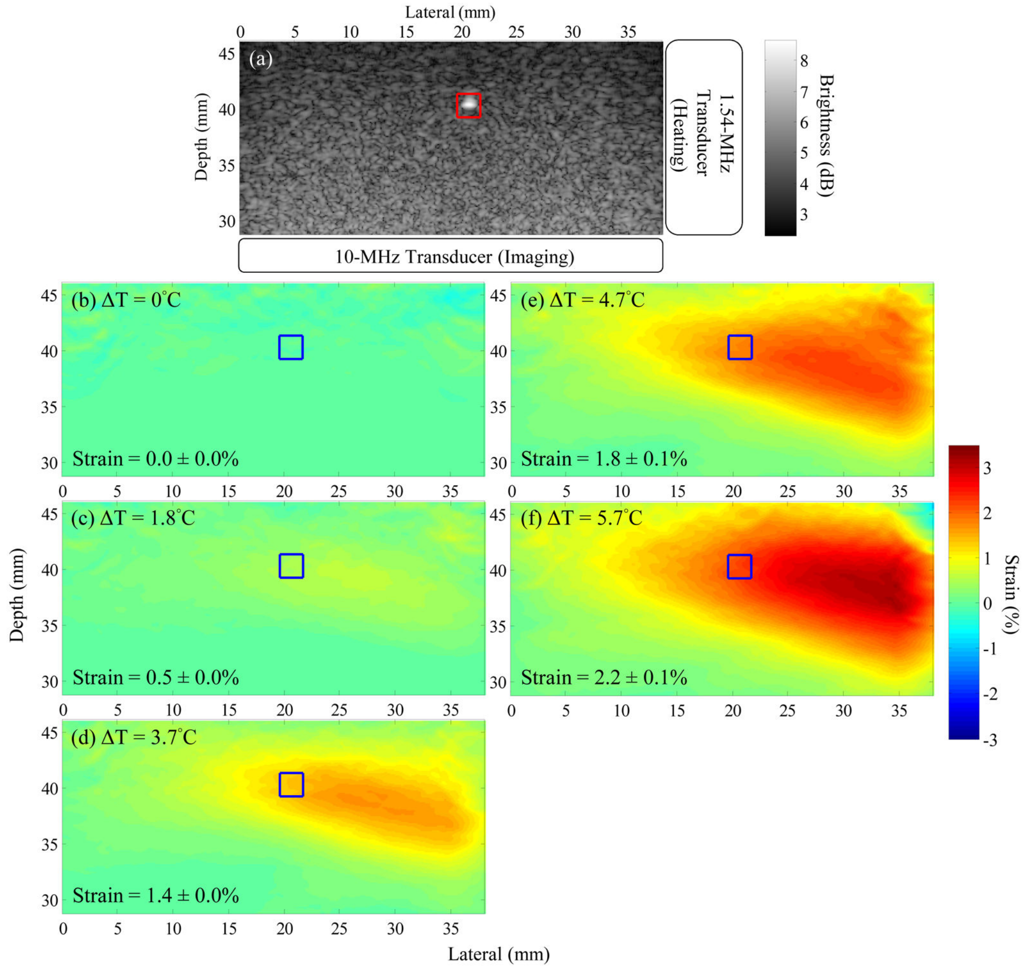

Fig. 6.

B mode image and thermal strain maps of the 30%-trioleate phantom. Parameters for the ROI and strain calculation were the same as in Fig. 5.

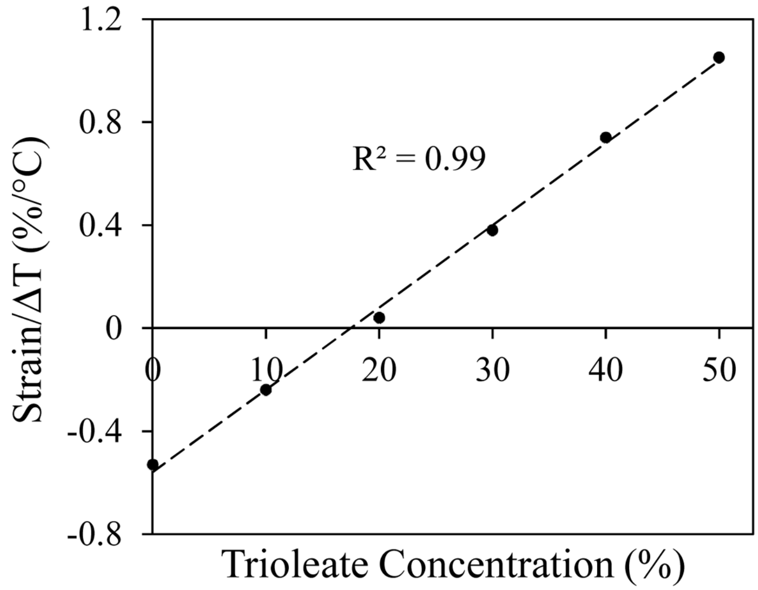

Fig. 7.

The inverse of the tissue dependent thermal strain parameter as a function of trioleate concentration.

NIH-PA Author Manuscript

NIH-PA Author Manuscript

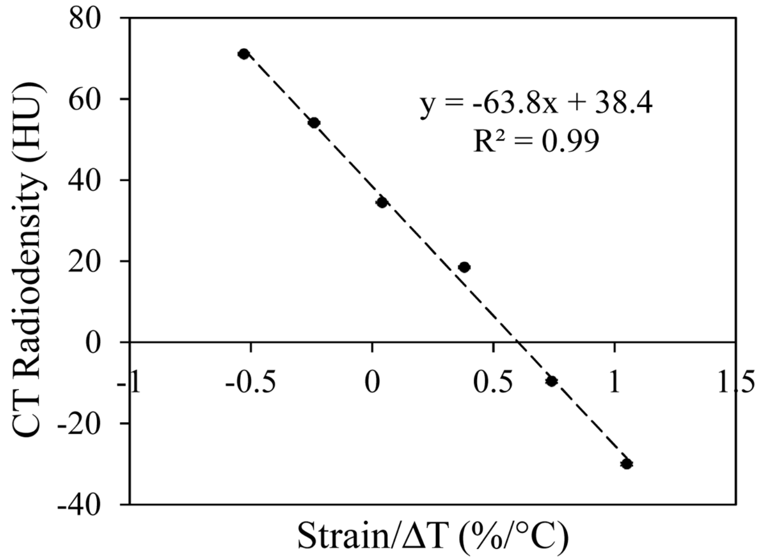

Fig. 8.

CT radiodensity as a function of the inverse of the tissue dependent thermal strain parameter. A high correlation was observed.

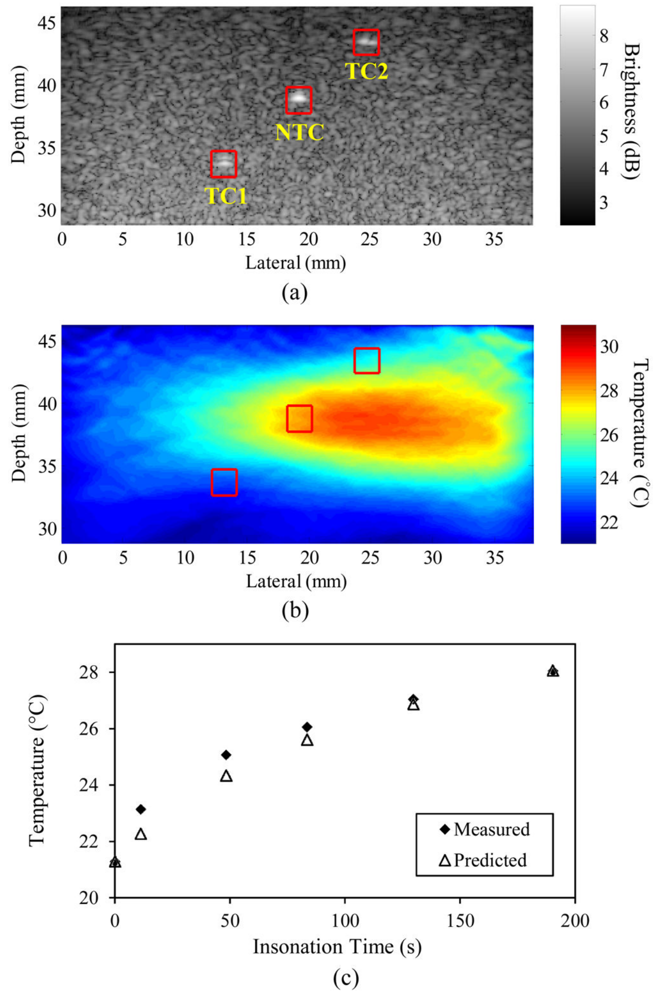

Fig. 9.

Temperature validation on a 25% trioleate phantom. (a) B mode image. (b) Predicted temperature map at the time point of maximum temperature increase at the needle thermocouple location (ΔT = 6.8°C). The locations of thermocouple #1 (TC1), thermocouple #2 (TC2), and the needle thermocouple (NTC) showed temperature prediction of 22.8, 25.0, and 28.1°C, compared to the measured temperatures of 23.3, 25.3, and 28.1°C, respectively. TC1 and TC2 were bare-junction thermocouples. The orientation is the same as in Figs. 5 and 6. The baseline temperature was 21.3°C. (c) Predicted and measured temperatures as a function of insonation time at the NTC location (plot of individual measurement is shown for clarity).

TABLE I

Phantom properties of 0 to 50% trioleate concentration

Trioleate concentration (%)	**0**	**10**	**20**	**30**	**40**	**50**
Density (g/cm^3) (n = 3)	1.06 ± 0.01	1.05 ± 0.01	1.04 ± 0.01	1.03 ± 0.01	1.02 ± 0.01	1.01 ± 0.01
SNR	1.94	1.88	1.92	1.95	1.93	1.89
CT radiodensity (HU) (n = 20)	71.1 ± 0.3	54.1 ± 0.3	34.5 ± 0.2	18.5 ± 0.3	−9.6 ± 0.4	−30.0 ± 0.4
Strain/ΔT (%/°C)	−0.53	−0.24	0.04	0.38	0.74	1.05

Note: Error shows one standard deviation.

TABLE II

SOS as a function of temperature for the phantoms with 0 to 50% trioleate concentration

Temperature (°C)	Water	Phantom, Trioleate concentration (%)					
		0	10	20	30	40	50
22.1	1470	1540 ± 0.1	1530 ± 0.2	1522 ± 0.6	1513 ± 0.1	1502 ± 0.2	1493 ± 0.2
26.3	1481	1547 ± 0.3	1534 ± 0.9	1522 ± 0.1	1510 ± 0.1	1497 ± 0.3	1485 ± 0.4
30.9	1492	1553 ± 0.4	1536 ± 0.2	1520 ± 0.3	1505 ± 0.2	1490 ± 0.4	1475 ± 0.8
35.7	1503	1560 ± 0.4	1539 ± 0.2	1519 ± 0.2	1500 ± 0.3	1481 ± 0.2	1464 ± 0.6
41.1	1513	1565 ± 0.5	1540 ± 0.3	1516 ± 0.5	1495 ± 0.4	1474 ± 1.1	1455 ± 1.1
ΔSOS/ΔT	2.3	1.3 ± 0.5	0.5 ± 0.4	−0.3 ± 0.7	−0.9 ± 0.4	−1.5 ± 1.1	−2.0 ± 1.1
R^2	0.99	0.99	0.96	0.92	0.99	0.99	0.99

Note: Unit of SOS: m/s. Unit of ΔSOS/ΔT: m/s/°C. The R^2 values show linear correlation between SOS and temperature. n = 4, error shows one standard deviation.

NIH-PA Author Manuscript

NIH-PA Author Manuscript

TABLE III

Accumulated temperature increase for RF data acquisition

Index	Trioleate concentration (%)					
	0	**10**	**20**	**30**	**40**	**50**
0	0.0	0.0	0.0	0.0	0.0	0.0
1	1.7	2.1	1.8	1.8	1.9	0.9
2	3.6	4.0	3.9	3.7	3.9	1.6
3	4.6	6.0	4.8	4.7	4.9	2.3
4	5.6	7.0	5.8	5.7	5.9	2.9
5	7.1	8.0	6.8		6.9	3.6
6			7.8			

Note: Unit of temperature: °C. Acquisition index 0 was the baseline temperature.

TABLE IV

Validation of additional phantoms

Trioleate concentration (%)	CT radiodensity estimated from Fig. 3 (HU)	Strain/ΔT predicted from Fig. 8 (%/°C)	Measured (actual) strain/ΔT (%/°C)	Absolute error of strain/ΔT (%/°C)	ΔT error, NTC (°C)	ΔT error, TC1 (°C)	ΔT error, TC2 (°C)
5	63.8	−0.40	−0.48	0.08	0.9 ± 0.7	0.7 ± 0.6	1.2 ± 0.8
25	23.1	0.24	0.23	0.01	0.4 ± 0.4	0.2 ± 0.2	0.2 ± 0.1
35	2.7	0.56	0.58	0.02	0.2 ± 0.2	0.4 ± 0.2	0.9 ± 0.6

Note: n = 6, error shows one standard deviation.

NIH-PA Author Manuscript
NIH-PA Author Manuscript

TABLE V

Measured and predicted temperature at the needle thermocouple (NTC) location in the three validation experiments

5% trioleate phantom				25% trioleate phantom				35% trioleate phantom			
Acq. ΔT	**Measured**	**Predicted**	**Error**	**Acq. ΔT**	**Measured**	**Predicted**	**Error**	**Acq. ΔT**	**Measured**	**Predicted**	**Error**
0.0	21.5	21.5	0.0	0.0	21.3	21.3	0.0	0.0	21.5	21.6	0.1
1.7	23.2	22.4	0.8	1.8	23.1	22.3	0.8	1.6	23.1	22.8	0.3
3.6	25.1	25.5	0.4	3.8	25.1	24.3	0.8	2.5	24.0	23.9	0.1
4.6	26.1	26.7	0.6	4.8	26.1	25.6	0.5	3.5	25.0	25.0	0.0
5.6	27.1	28.3	1.2	5.8	27.1	26.9	0.2	4.5	26.0	26.2	0.2
6.5	28.0	30.1	2.1	6.8	28.1	28.1	0.0	5.5	27.0	27.5	0.5
		Mean of error:	0.9			Mean of error:	0.4			Mean of error:	0.2
		Std of error:	0.7			Std of error:	0.4			Std of error:	0.2

Note: The baseline temperature of the 5%, 25%, and 35% cases was 21.5, 21.3, and 21.5°C, respectively. The error between measured and predicted temperature was absolute error. The unit of temperature was °C. “Acq.” denotes “acquisition”.